ANALYTICAL SOLUTION OF THE EULER EQUATIONS FOR AIRFOIL FLOW AT SUBSONIC AND TRANSONIC CONDITIONS

A. Verhoff
Consultant, Fluid Dynamics
Saint Louis, Missouri, US

Abstract

A compact formulation for obtaining analytical solutions of the 2D steady-state Euler equations is presented. The equations are formulated in the physical plane with flow angle and logarithm of isentropic momentum magnitude as dependent variables. Higher-order effects (e.g., compressibility and entropy) appear as non-homogeneous forcing terms. The solution procedure does not require a Green's function for the forcing terms and has general applicability to many other disciplines (e.g., heat transfer) besides fluid dynamics. The zero-order approximation is obtained from solution of the linear, homogeneous system (a boundary-value problem on a simple domain), and is remarkably accurate into the transonic range. Higher-order corrections are generated by iterating on the non-homogeneous terms. Application of the solution approach combined with specialized shock mappings allows analytical transonic flow solutions with a shock wave. The Rankine-Hugoniot shock relations are enforced across the discontinuity along with the correct entropy change. Generation of the analytical solutions is facilitated by the *Mathematica* symbolic manipulation software. Results are presented that demonstrate the potential accuracy and simplicity of the new procedure.

1 Introduction

Many well-known classical analytical techniques have been developed over the past several centuries that can form the framework for very powerful and elegant methods of solution of boundary value problems. Application of these methods after inception, however, was limited to very simple problems (i.e., simple boundary shapes) because quantitative numerical results could only be achieved by tedious hand-calculation. Since the arrival of digital computers at the middle of the last century, research has focused primarily on discrete methods for the solution of complex boundary value problems. Little attention has been paid to integrating the classical methods into analysis tools to take advantage of the efficiency and physical modeling accuracy they can provide. Over the past 15 years a limited research program has focused on demonstrating and evaluating the coupling of analytical and numerical methods ([1], [2] ,[3], and [4]). The current state of one phase of this effort is described in this paper.

An approach was introduced in [2] for obtaining analytical asymptotic solutions of the two-dimensional (2D) steady-state Euler equations in streamline coordinates. The equations were written such that higher-order compressibility and rotational effects appeared as right-hand-side (RHS) forcing terms. A complex-variable mapping was then applied to this non-homogeneous Cauchy-Riemann system which contracts the Euler equations into a single first-order partial differential equation (PDE) in the complex plane. This single PDE was solved by asymptotic iterative correction whereby the RHS terms were evaluated using lower-order, previous-iteration approximations. The basis for this iterative approach was the binomial expansion of the density and mass flux relations, which are convergent for all Mach numbers and rapidly convergent well into the supersonic range.

The procedure was applied to transonic (shock free) flow past a circular cylinder in [2]. The asymptotic solution was generated (derived) to seventh order using a *Mathematica* solver algorithm. Solution accuracy was validated by the gas-dynamic mass flux condition at sonic points and critical Mach number prediction. The solution method was subsequently applied [3] to compressible flow past a ramp (or wedge-type) geometry to clarify inviscid flow behavior near geometric singularities. This solution was shown likewise to extend into the transonic (shock free) range. Its accuracy was validated by comparison with experimental results. Excellent corroboration with the von Karman similarity rule was also demonstrated. More recently, the procedure was applied to compressible airfoil flow [4], where very efficient analytical generation of design sensitivity derivatives was demonstrated. However, the Euler equations were solved in streamline coordinates, which had a number of drawbacks in terms of the required mappings.

The improved procedure described herein uses physical coordinates, eliminating the mapping to the streamline plane. The formulation is compact in that the RHS terms are minimal and their functional form similar for each equation. The dependent variables are flow angle and logarithm of isentropic momentum magnitude (relative to free stream value), a consequence of the compact form and the use of physical coordinates. Use of flow angle simplifies imposition of surface and far-field boundary conditions. The variable dependent on momentum contains a substantial portion of the (nonlinear) flowfield compressibility effects and yields much improved accuracy at comparable solution order. This new form of the Euler equations is again expressed as a non-homogeneous Cauchy-Riemann system and the solution procedure of [2] is applicable. Using only the surface geometry definition (i.e., no computational grid), the solution provides the full flowfield description.

The choice of flow angle as a dependent variable leads to a stronger set of boundary conditions for a given problem. At a solid surface the usual inviscid condition of tangential flow (i.e., zero normal velocity) does not fix the velocity direction, leading to the necessity of a Kutta condition to remove the ambiguity. Tangential flow with a prescribed direction can be imposed when flow angle is used.

The complex-variable mapping used previously is applied to the present non-homogeneous Cauchy-Riemann system resulting in a single first-order PDE in the complex plane. This solution procedure allows closed-form analytical solutions of this PDE, provided the RHS terms are analytically defined. In this case the solution procedure is reduced to evaluation of indefinite integrals. The generated sequence of corrections is not asymptotic in the traditional sense; neglecting higher-order corrections only reduces accuracy and does not compromise physics. Introduction of a local shock mapping allows discontinuities (Rankine-Hugoniot) occurring at a shock wave to be incorporated as standard Dirichlet boundary conditions and shock position determined.

The PDE solution procedure is general and applicable to the Poisson equation and its various subsets, such as the non-homogeneous Cauchy-Riemann system arising in the present analysis, and also the non-homogeneous bi-harmonic equation. It therefore has applicability to many other disciplines, such as heat transfer, structures, etc.

Subsonic and transonic results are presented that demonstrate the potential accuracy and efficiency of the new formulation. These include Karman-Trefftz airfoil solutions and a bi-convex airfoil solution with and without a shock wave.

2 Analytical Formulation

For 2D steady flow the Euler equations can be written in physical (x,y) coordinates as

$$\begin{aligned}
&\frac{\partial\theta}{\partial x}-\frac{\partial Q}{\partial y}=-\frac{1}{2}M^2\sin 2\theta[\frac{\partial Q}{\partial x}+\tan\theta\frac{\partial Q}{\partial y}]+\frac{1}{M^2}\frac{\partial S}{\partial y}\\
&\frac{\partial\theta}{\partial y}+(1-M^2)\frac{\partial Q}{\partial x}=\frac{1}{2}M^2\sin 2\theta[\frac{\partial Q}{\partial y}-\tan\theta\frac{\partial Q}{\partial x}]-\frac{1}{M^2}\frac{\partial S}{\partial x}\\
&\cos\theta\frac{\partial S}{\partial x}+\sin\theta\frac{\partial S}{\partial y}=0\\
&a^2+\frac{\gamma-1}{2}q^2=1
\end{aligned}\qquad (1)$$

The flow angle is θ (with $\theta_\infty = 0$), Q is the logarithm of velocity magnitude q, the local Mach number is M, and the speed of sound is a. Velocities are non-dimensionalized by stagnation speed of sound, and pressure and density by their respective stagnation values. Note the energy equation is algebraic for steady flow. Entropy S is convected along streamlines and is defined in terms of pressure p and density ρ as

$$S \equiv \frac{1}{\gamma(\gamma-1)} \ln\left(\frac{p}{\rho^\gamma}\right) \tag{2}$$

Density can be expressed as a function of velocity magnitude and entropy according to

$$\rho = [1 - \frac{\gamma-1}{2} q^2]^{1/(\gamma-1)} \, e^{-\gamma S} \tag{3}$$

For constant far-field pressure p_∞, reference quantities can be defined as

$$\begin{aligned} \bar{a}_\infty &\equiv (p_\infty)^{(\gamma-1)/2\gamma} \\ \bar{q}_\infty &\equiv \sqrt{\frac{2}{\gamma-1}(1-\bar{a}_\infty^2)} \\ \bar{M}_\infty &\equiv \bar{q}_\infty / \bar{a}_\infty \end{aligned} \tag{4}$$

These constant quantities can be associated with the upstream isentropic conditions. Then

$$\begin{aligned} a_\infty^2 &= \bar{a}_\infty^2 e^{(\gamma-1)S_\infty} \\ q_\infty^2 &= \frac{2}{\gamma-1}[1 - \bar{a}_\infty^2 e^{(\gamma-1)S_\infty}] \\ M_\infty^2 &= \frac{2}{\gamma-1}[(1 + \frac{\gamma-1}{2}\bar{M}_\infty^2) e^{(1-\gamma)S_\infty} - 1] \end{aligned} \tag{5}$$

From the second of Eqs.(5)

$$\begin{aligned} \frac{1}{M_\infty^2}\frac{\partial S_\infty}{\partial y} &= -\frac{1}{2}\frac{\partial}{\partial y}\ln[1 - \bar{a}_\infty^2 e^{(\gamma-1)S_\infty}] = -\frac{\partial}{\partial y}\ln[q_\infty] \\ \frac{1}{M_\infty^2}\frac{\partial S_\infty}{\partial x} &= -\frac{\partial}{\partial x}\ln[q_\infty] = 0 \end{aligned} \tag{6}$$

Note that q_∞ depends only on y for non-isentropic conditions, since $\theta_\infty = 0$. Using these results Eqs.(1) become (after some manipulation)

$$\begin{aligned} \frac{\partial\theta}{\partial x} - \frac{\partial J}{\partial y} &= \cos 2\theta \frac{\partial R}{\partial y} - \sin 2\theta \frac{\partial R}{\partial x} + \frac{1}{M^2}\frac{\partial S}{\partial y} \\ &\quad + \sin^2\theta \frac{\partial S_\infty}{\partial y} - \frac{1}{M_\infty^2}\frac{\partial S_\infty}{\partial y} \\ \frac{\partial\theta}{\partial y} + \frac{\partial J}{\partial x} &= \cos 2\theta \frac{\partial R}{\partial x} + \sin 2\theta \frac{\partial R}{\partial y} - \frac{1}{M^2}\frac{\partial S}{\partial x} \\ &\quad - \sin\theta\cos\theta \frac{\partial S_\infty}{\partial y} + \frac{1}{M_\infty^2}\frac{\partial S_\infty}{\partial x} \end{aligned} \tag{7}$$

The functions J and R in this compact form are defined as

$$\begin{aligned} J \equiv \frac{1}{2}\ln[q^2(1-\frac{\gamma-1}{2}q^2)^{1/(\gamma-1)}] \\ -\frac{1}{2}\ln[q_\infty^2(1-\frac{\gamma-1}{2}q_\infty^2)^{1/(\gamma-1)}] \end{aligned} \tag{8}$$

$$R \equiv -\frac{1}{2}\ln[(1-\frac{\gamma-1}{2}q^2)^{1/(\gamma-1)}] + \frac{1}{2}\ln[(1-\frac{\gamma-1}{2}q_\infty^2)^{1/(\gamma-1)}] \tag{9}$$

The variable J represents the logarithm of isentropic momentum magnitude relative to free stream value, and includes a substantial portion of the flowfield compressibility effects. Eqs.(5) provide for far-field entropy variation. For non-isentropic conditions, q_∞ depends on S_∞ (e.g., in the far-field wake of a shock wave). In the far field θ_∞ and J_∞ both vanish.

The relative magnitude of R as a function of local Mach number is shown in Fig. 1, with free stream Mach number as a parameter. The ratio is relatively small up to moderate free stream Mach numbers, so that solution of the homogeneous portion of Eqs.(7) can yield a good approximation. For higher Mach numbers the non-homogeneous equations should be solved. Typically, flow angle is small throughout most of a flowfield, so that some of the RHS terms can be ignored if total accuracy is not required.

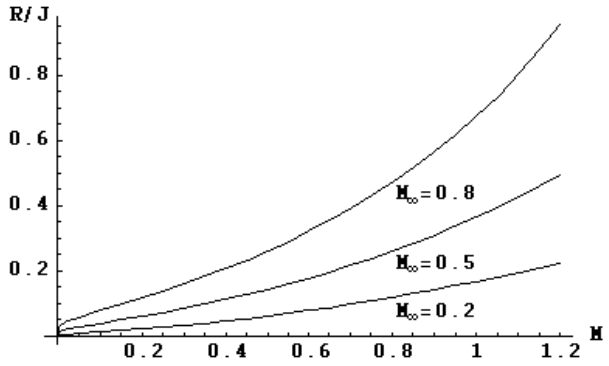

Fig. 1 Relative Magnitude of R as a Function of Local Mach Number ($\gamma = 7/5$)

The system (7) can be viewed as linear, constant-coefficient, non-homogeneous partial differential equations, assuming that the RHS terms are known quantities. The system can be solved by iteration and these terms, if reasonably small and well-behaved, can be approximated using previous iteration results. (Previous asymptotic analyses support this assumption.) Solution of the ho-

mogeneous left-hand-side (LHS) portion provides an initial starting approximation.

3 Solution Procedure

The solution process introduced in [2] for the non-homogeneous equations is outlined below. It can utilize conformal mappings (for accurate imposition of boundary conditions), integral transforms, asymptotic methods, etc., depending on the problem being addressed. Provided the RHS terms are analytically defined, closed-form analytical solutions can be obtained readily even when the RHS terms are functionally complicated. A Green's function is not required.

Introduction of the new complex dependent variable

$$F \equiv J - i\theta \tag{10}$$

and the complex-variable mapping

$$x = \frac{1}{2}(\bar{z} + z) \qquad y = \frac{i}{2}(\bar{z} - z)$$
$$z \equiv x + iy \qquad \bar{z} \equiv x - iy \tag{11}$$

contracts the Euler system (7) into the single first-order PDE

$$\frac{\partial F}{\partial \bar{z}} = e^{2i\theta}\frac{\partial R}{\partial z} + \Psi \tag{12}$$

The explicit entropy terms are represented by the quantity Ψ, defined as

$$\Psi \equiv \left(\frac{1}{M_\infty^2} - \sin^2\theta\right)\frac{\partial S_\infty}{\partial \bar{z}} - \frac{1}{M^2}\frac{\partial S}{\partial \bar{z}} - \frac{i}{4}\sin 2\theta\left(\frac{\partial S}{\partial z} - \frac{\partial S}{\partial \bar{z}}\right) \tag{13}$$

Integration of Eq.(12) gives

$$F(z,\bar{z}) = \int\left[e^{2i\theta}\frac{\partial R}{\partial z} + \Psi\right]d\bar{z} + H(z) \tag{14}$$

where the homogeneous solution $H(z)$ provides the means for imposing both surface and far-field boundary conditions.

If a conformal mapping represented by

$$z = G(\zeta) \qquad \zeta \equiv \xi + i\eta \tag{15}$$

is introduced, Eq.(12) becomes

$$\frac{\partial F}{\partial \bar{\zeta}} = \frac{d\bar{G}}{d\bar{\zeta}}\left[e^{2i\theta}\frac{\partial R}{\partial \zeta}\left(\frac{dG}{d\zeta}\right)^{-1} + \Psi\right] \tag{16}$$

Formal integration yields

$$F(\zeta,\bar{\zeta}) = \int\frac{d\bar{G}}{d\bar{\zeta}}\left[e^{2i\theta}\frac{\partial R}{\partial \zeta}\left(\frac{dG}{d\zeta}\right)^{-1} + \Psi\right]d\bar{\zeta} + H(\zeta) \tag{17}$$

Such a mapping can be used to transform to a suitable computational plane. A first approximation (zero-order) to the solution of Eqs.(14) or (17) is obtained by setting R and Ψ to zero, so that any analytic function of z (or ζ) that satisfies the boundary conditions can be selected. This zero-order approximation, which contains some compressibility effects, can then be used to approximate R and Ψ. Subsequent solution of Eqs.(14) or (17) generates an improved approximation. Iteration can be continued to achieve desired accuracy.

If a non-conformal mapping represented by

$$z = G(\zeta,\bar{\zeta}) \qquad \bar{\zeta} \equiv \xi - i\eta \tag{18}$$

is introduced rather than the mapping (15), the Euler system (7) becomes

$$\frac{\partial F}{\partial \bar{\zeta}} = \left(\frac{\partial G}{\partial \zeta}\right)^{-1}\left\{\frac{\partial F}{\partial \zeta}\frac{\partial G}{\partial \bar{\zeta}} + e^{2i\theta}\left[\frac{\partial \bar{G}}{\partial \bar{\zeta}}\frac{\partial R}{\partial \zeta} - \frac{\partial \bar{G}}{\partial \zeta}\frac{\partial R}{\partial \bar{\zeta}}\right] + \Psi\right\} \tag{19}$$

This expression is slightly more complicated than Eq.(16) for the case of a conformal mapping. This type of specialized mapping was used in the analysis of [3]. For a non-conformal mapping of coordinate-straining type, the function G can be represented by the expansion

$$z = \zeta + \varepsilon G_1(\zeta,\bar{\zeta}) + \varepsilon^2 G_2(\zeta,\bar{\zeta}) + \cdots \tag{20}$$

where ε is a small mapping parameter. This justifies including the ζ–derivative of F with the higher-order terms.

The process outlined above is systematic and can be programmed for symbolic manipulation software such as *Mathematica*. For example [2], the seventh-order analytical solution for flow past a circular cylinder was computer derived. Solution results into the low transonic (shock free) range could then be generated from functional evaluations.

Each order of correction generated by Eqs.(14) or (17) is done so by using only lower-order results, and does not alter the lower-order results. The expansion thus generated is not asymptotic in the traditional sense. Typically, an asymptotic expansion represents the departure from some baseline solution, the extent depending on the magnitude of a small expansion parameter. The baseline solution is independent of the expan-

sion parameter. When the expansion parameter vanishes or the higher-order terms are neglected, the baseline solution remains. For example, in the case of the Janzen-Rayleigh formulation (see [5]), the incompressible solution is recovered when either M_∞ approaches zero or the higher-order terms are neglected. In the present formulation, the incompressible solution is obtained as M_∞ approaches zero. However, neglecting the higher-order terms leaves a zero-order solution that is strongly influenced by M_∞. This will be evident in the results presented below.

4 Circular Cylinder Application

The solution procedure outlined above will be demonstrated for the simple problem of compressible shock-free flow past a circular cylinder. Results are compared at sub-critical Mach number with the asymptotic solution results of [2]. Critical Mach number is also predicted.

The zero-order (homogeneous) solution can be obtained by mapping the physical plane exterior to the cylinder to a semi-infinite strip in the $\zeta-$plane $(|\xi|\le\pi;\eta\ge 0)$. This is accomplished by the mapping

$$\begin{aligned} z &= e^{-i\zeta} \\ &= e^{\eta}(\cos\xi - i\sin\xi) \end{aligned} \tag{21}$$

This mapping is illustrated in Fig. 2 for a unit circle. The solution is periodic in the $\zeta-$plane. In terms of polar coordinates

$$z = re^{i\omega} = \sqrt{x^2+y^2}\,(\cos\omega + i\sin\omega) \tag{22}$$

Comparison of this expression with Eq.(21) implies

$$\begin{aligned} r &= e^{\eta} = \sqrt{x^2+y^2} \\ \omega &= -\xi = \tan^{-1}(y/x) \qquad (-\pi\le\omega\le\pi) \end{aligned} \tag{23}$$

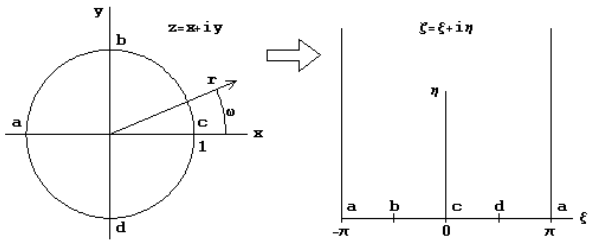

Fig. 2 Mapping to Semi-Infinite Strip

The boundary distribution of surface flow angle θ_b is transferred to the base of the strip as shown in Fig. 3. The analytic function with this

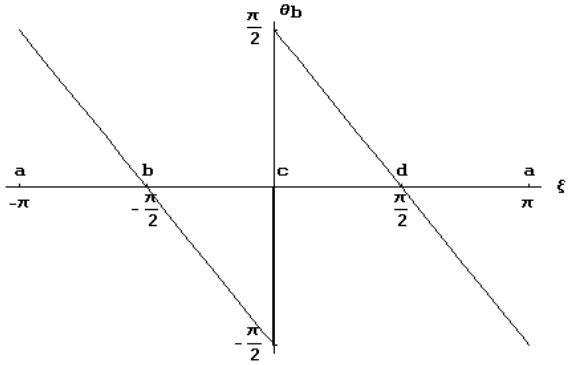

Fig. 3 Surface Boundary Conditions

base distribution is obtained from the Fourier representation

$$\theta_b = \sum_{k=1}^{\infty}\frac{1}{k}[1+(-1)^k]\sin k\xi \tag{24}$$

Using the relations

$$\begin{aligned} \log[1+e^{i\zeta}] &= -\sum_{k=1}^{\infty}\frac{(-1)^k}{k}e^{i\zeta} \\ \log[1-e^{i\zeta}] &= -\sum_{k=1}^{\infty}\frac{1}{k}e^{i\zeta} \end{aligned} \tag{25}$$

it follows that

$$\mathrm{Imag}\{\log[1-e^{2i\zeta}]\} = -\sum_{k=1}^{\infty}\frac{1}{k}[1+(-1)^k]e^{-k\eta}\sin k\xi \tag{26}$$

Comparison with Eq.(24) at η=0 provides the zero-order solution

$$\begin{aligned} F_0 = J_0 - i\theta_0 &= \log[1-e^{2i\zeta}] \\ &= \log\left[1-\frac{1}{z^2}\right] \end{aligned} \tag{27}$$

Note that z and ζ are related by the mapping (21). The real and imaginary parts of F_0 are

$$J_0 = \frac{1}{2}\log\left[\left(1-\frac{1}{z^2}\right)\left(1-\frac{1}{\bar{z}^2}\right)\right] \tag{28}$$

and

$$\theta_0 = \frac{i}{2}\left\{\log\left[1-\frac{1}{z^2}\right] - \log\left[-\frac{1}{\bar{z}^2}\right]\right\} \tag{29}$$

On the cylinder surface (η=0)

$$J_b = \ln[2|\sin\xi|] \tag{30}$$

and

$$\theta_b = \tan^{-1}[\cot \xi] \qquad (31)$$

For incompressible flow (i.e., $M_\infty \to 0$) these component solutions are equivalent to the classical circular cylinder solution, since the RHS forcing terms vanish (see Fig. 1).

Knowing the spatial functions J_0 or J_b from Eqs.(28) or (30), then for a given free stream Mach number velocity magnitude q is obtained from Eq.(8), after which all other fluid dynamic variables can be determined. Note that these relations provide a description of the entire flowfield.

The surface Mach number variation (with arc length σ) obtained from the zero-order solution (30) is compared in Fig. 4 with the analytical, fourth-order asymptotic solution results of [2]. The free stream Mach number is 0.25. The asymptotic solution has a slightly lower peak Mach number and is very accurate at this condition. The zero-order solution agrees well with the fourth-order solution which is indicative of the inherent accuracy of the present formulation.

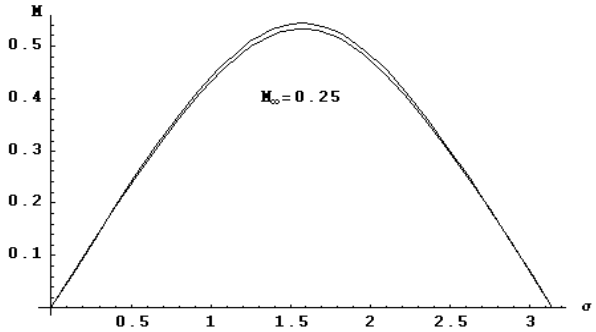

Fig. 4 Surface Mach Number Solution Comparison

The zero-order-solution Mach number distribution for which sonic conditions are reached at the top of the cylinder is shown in Fig. 5. The value of M_∞ is 0.382 (i.e., predicted critical Mach number); critical Mach number for a cylinder is 0.40. The accuracy of this result (within 5 percent) is remarkable, having been obtained from the solution of a Cauchy-Riemann (linear, homogeneous) system.

Surface Mach number distribution (as a function of arc length) predicted by the first-order solution for a free stream Mach number of 0.25 is shown in Fig. 6. Also shown is the fourth-order asymptotic solution appearing in Fig. 4. The two solutions agree very closely; the asymptotic solution has a slightly lower peak Mach number. The critical Mach number predicted by the first-order solution is 0.392 (2 percent error).

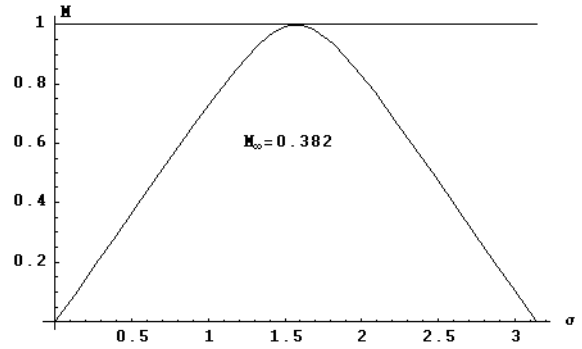

Fig. 5 Critical Mach Number Prediction

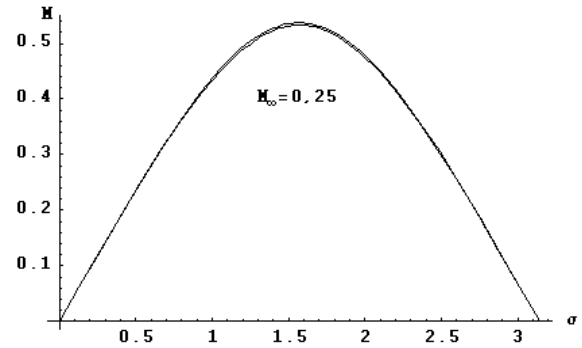

Fig. 6 Surface Mach Number Solution Comparison

5 Airfoil Application

Analytical formulation accuracy can be further validated by comparing results with classical incompressible Karman-Trefftz airfoil solutions and to some extent with CFD solutions for arbitrary airfoil shapes. A typical Karman-Trefftz airfoil is shown in Fig. 7. The included trailing edge angle is 10 degrees and the thickness is 10 percent.

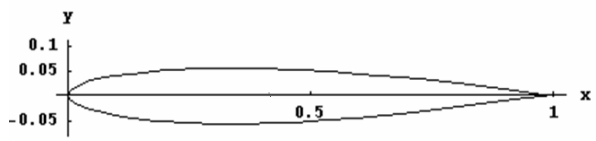

Fig. 7 Karman-Trefftz Airfoil

At incompressible conditions (i.e., $M_\infty \to 0$) results from the present formulation differ from classical (exact) Karman-Trefftz solutions by less than 10^{-4} for arbitrary angle of attack. Note that

RHS forcing terms are non-zero only for compressible flow. Critical Mach number for the airfoil of Fig. 7 at 2 degrees incidence predicted by the zero-order solution is 0.65, as shown in Fig. 8.

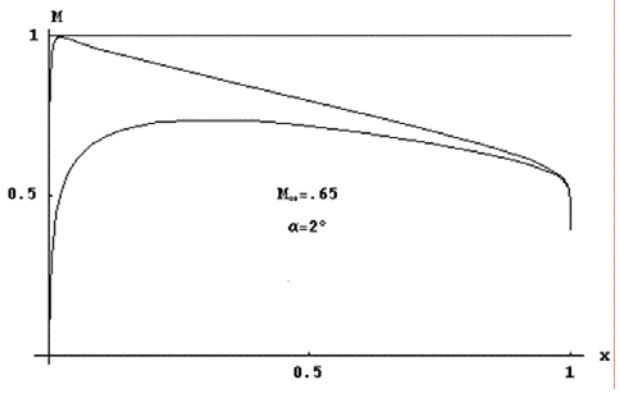

Fig. 8 Surface Mach Number Distribution

A comparison of zero-order results with a CFD Euler solution for a NACA 0012 airfoil at zero incidence is shown in Fig. 9. The free stream Mach number is 0.70. Agreement is good considering the CFD results were generated with a coarse unstructured grid having 30 nodes on the airfoil surface. Analytically predicted critical Mach number is 0.73, which is within 2 percent of that predicted by a fine-grid CFD solution.

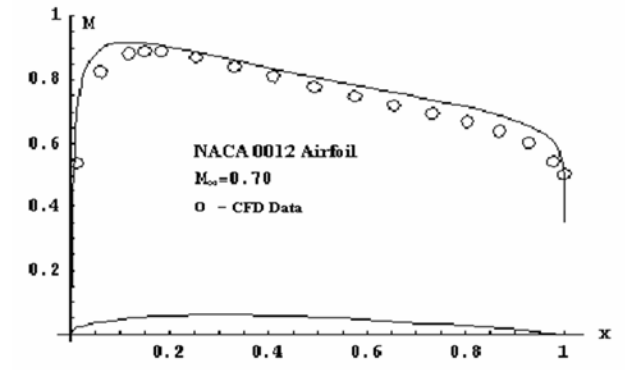

Fig. 9 Comparison of Surface Mach Number Predictions

6 Shock Wave Description

The zero-order Euler solution (solution of the homogeneous equation) is given in terms of analytic functions, while the higher-order correction terms involve non-analytic functions. Analytic functions are adequate for predicting gross (zero-order) flowfield features, such as flow behavior at a stagnation point or sharp trailing edge. A shock wave is normally a zero-order effect. Within the analytic-function framework, a discontinuity in surface flow angle θ_b produces a surface singularity in J_b (typically logarithmic), such as at a stagnation point. Conversely, a surface discontinuity in J_b (as at a shock wave) produces a singularity in θ_b, which is physically inconsistent.

For a transonic flow with an embedded shock wave, the shock is normal at the surface if the surface is smooth, and θ_b is constant across the shock, even though J_b is discontinuous. The body surface can be mapped conformally by a number of procedures onto a portion of the real axis of some intermediate $\phi-$plane, where

$$\phi \equiv \lambda + i\mu \tag{32}$$

Surface flow-angle boundary conditions are transferred to the real axis. The surface location at the foot of the shock is denoted by z_* in the physical plane and λ_* denotes its image in the $\phi-$plane. A strategy for describing a transonic flowfield with a shock wave is to include the shock as part of the computational-plane boundary on which boundary conditions are prescribed. On this portion conditions are provided by the Rankine-Hugoniot shock relations. A very local conformal mapping which emulates a shock-like structure is

$$\zeta = \lambda_* \pm \sqrt{(\phi-\lambda_*)^2+\delta^2} \qquad \zeta \equiv \xi + i\eta \tag{33}$$

The mapping parameter δ is equal to the shock height. This mapping is illustrated in Fig. 10. The shock is represented by the segment *abc*. Points *a* and *c* lie at $\lambda=\lambda_*$ on the real axis in the $\phi-$plane. In the $\zeta-$plane, point *b* lies at $\xi=\xi_*$ and points *a* and *c* at $\xi=\xi_* \mp \delta$, respectively.

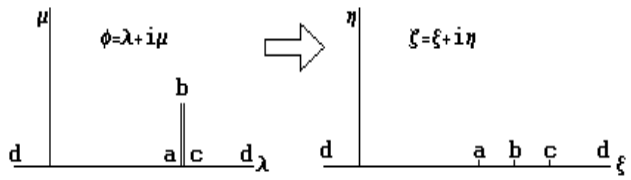

Fig. 10 Shock Wave Mapping

The inverse of this spike mapping is

$$\phi = \xi_* \pm \sqrt{(\zeta-\xi_*)^2-\delta^2} \tag{34}$$

Note that $\xi_*=\lambda_*$. The image of constant $\mu-$lines in the $\zeta-$plane is shown in Fig. 11 for small val-

ues of μ. The variation of λ along the real axis ($\eta = 0$) is shown in Fig. 12.

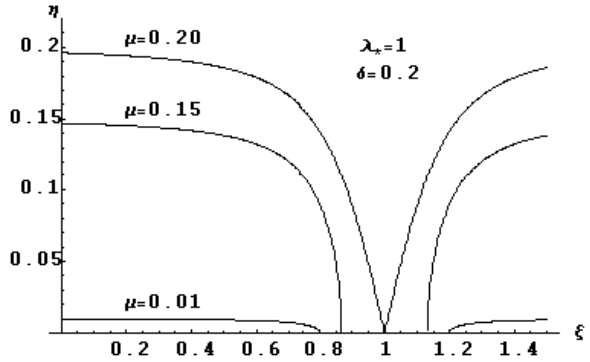

Fig. 11 Variation of η Near Boundary

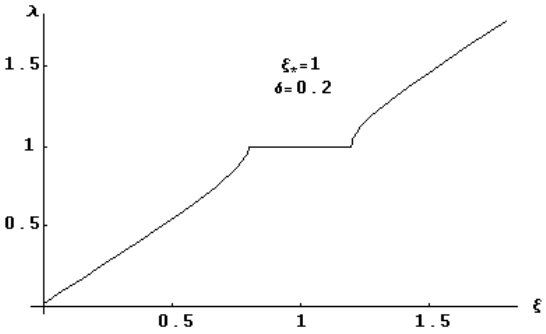

Fig. 12 Variation of λ Along Real Axis

A local non-conformal mapping, as discussed in connection with Eq.(19), can be introduced in the vicinity of the shock wave to account for shock curvature. This process introduces RHS forcing terms.

The parameter δ can be chosen so that the jump conditions across the shock at the surface agree with the normal shock relations. The surface entropy change across the shock can be approximated [6] for moderate shock strength by

$$\Delta S = \frac{2}{3(\gamma+1)^2}(M_1^2 - 1)^3 \qquad (35)$$

where M_1 is the upstream shock Mach number. Since entropy is convected unchanged along the wetting streamline to infinity, $S_\infty = \Delta S$ and the Mach number at infinity on this streamline can be approximated by

$$M_\infty^2 = \overline{M}_\infty^2 - 2\left(1 + \frac{\gamma-1}{2}\overline{M}_\infty^2\right)S_\infty \qquad (36)$$

The quantity $\overline{M}_\infty$ is the upstream isentropic (reference) Mach number, as defined by Eqs.(4). Similar treatment is applied to off-body streamlines passing through the shock wave.

7 Bi-Convex Airfoil Application

The shock wave formation mechanism outlined above is illustrated for the case of flow past a thin bi-convex airfoil at zero incidence. The analysis is carried out at the zero-order level.

A bi-convex airfoil of thickness t can be approximated by

$$y = t(1 - x^2) \;;\; |x| \le 1 \qquad (37)$$

The leading and trailing edges are at $x = \mp 1$, respectively, as shown in Fig. 13 for the case t=0.10. The surface flow angle is

$$\theta_b = \tan^{-1}\left[\frac{dy}{dx}\right] \approx -2tx \qquad (38)$$

For t=0.15 the approximation error is less than 0.3 percent.

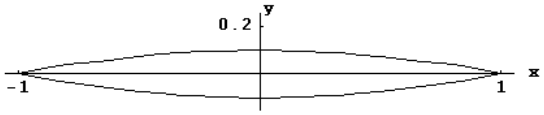

Fig. 13 Bi-Convex Airfoil Geometry

Using the approximation (38) combined with the "slender-body" approximation (i.e., boundary conditions applied on the real axis instead of the body surface), the zero-order solution for zero angle of attack can be obtained from the Poisson Integral Formula, namely,

$$F_0 = \frac{2t}{\pi} z \log\left[\frac{z-1}{z+1}\right] + \frac{4t}{\pi} \qquad (39)$$

The constant term has been added to satisfy the condition that F vanish at infinity. The real and imaginary parts of F_0 on the boundary (y=0) are

$$J_b = \frac{t}{\pi} x \ln\left[\left(\frac{x-1}{x+1}\right)^2\right] + \frac{4t}{\pi} \qquad (40)$$

and

$$\theta_b = \frac{2t}{\pi} x \lim_{y \to 0}\left[\tan^{-1}\left(\frac{y}{x+1}\right) - \tan^{-1}\left(\frac{y}{x-1}\right)\right] \qquad (41)$$

The error introduced by the slender-body approximation is small (for small t) and can be compensated for by a shearing transformation in the physical plane. Such a transformation is non-conformal and gives rise to RHS terms, as discussed in connection with Eq.(19).

Zero-order Mach number distributions for t=0.15 are shown in Fig. 14 for $M_\infty = 0.20$ and the case where sonic conditions are reached at the maximum thickness point (x=0). The predicted critical Mach number is 0.71. Numerical solution results are also shown. Both solutions (CFD and simplified analytical) predict almost the same critical Mach number and generally agree well, which is indicative of the lesser importance of the RHS forcing terms. The relatively coarse H-grid (90x30) used for the CFD solutions had 30 points on the surface. Note the change in distribution shape due to compressibility as the free stream Mach number increases.

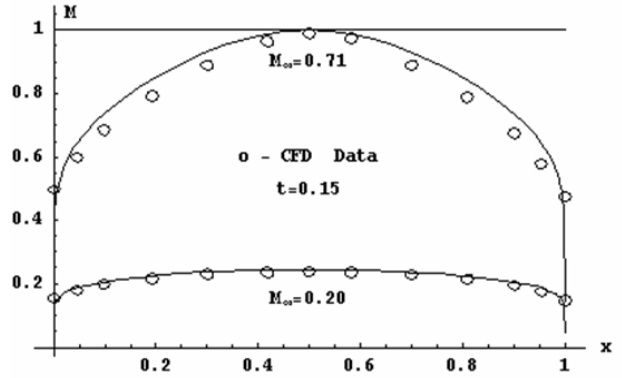

Fig. 14 Comparison of Surface Mach Number Predictions

For the transonic flow case, the inverse mapping (34) provides the variation (see Fig. 12) of x along the real axis of the computational ζ – plane, namely,

$$x = x_* + Sign[\xi - x_*]\,Real\{\sqrt{(\xi - x_*)^2 - \delta^2}\} \quad (42)$$

The image of the leading and trailing edge points are

$$\xi_{le} = x_* - \sqrt{(1 + x_*)^2 + \delta^2} \quad (43)$$

$$\xi_{te} = x_* + \sqrt{(1 - x_*)^2 + \delta^2} \quad (44)$$

Using the approximation noted in Eq.(38), the flow angle boundary conditions upstream and downstream of the shock may be written

$$\begin{aligned} \theta_b &= -2t[x_* - \sqrt{(\xi - x_*)^2 - \delta^2}\,] \quad ; \xi_{le} \le \xi \le x_* - \delta \\ \theta_b &= -2t[x_* + \sqrt{(\xi - x_*)^2 - \delta^2}\,] \quad ; \xi_{te} \ge \xi \ge x_* + \delta \end{aligned} \quad (45)$$

Various levels of approximation can be applied over the shock portion of the boundary. Using a quadratic-type distribution, application of the Poisson Integral Formula gives the solution in the form

$$\begin{aligned} F_0 = \frac{2t}{\pi}\{ & x_* \int_{\xi_{le}}^{\xi_{te}} \frac{d\sigma}{\sigma - \zeta} + \varepsilon \int_{x_* - \delta}^{x_*} \frac{(\sigma - x_*)(\sigma - x_* + \delta)}{\sigma - \zeta} d\sigma + \\ & \varepsilon \int_{x_*}^{x_* + \delta} \frac{(\sigma - x_*)(\sigma - x_* - \delta)}{\sigma - \zeta} d\sigma - \\ & \int_{\xi_{le}}^{x_* - \delta} \sqrt{(\sigma - x_*)^2 - \delta^2}\, \frac{d\sigma}{\sigma - \zeta} + \\ & \int_{x_* + \delta}^{\xi_{te}} \sqrt{(\sigma - x_*)^2 - \delta^2}\, \frac{d\sigma}{\sigma - \zeta} \} \end{aligned} \quad (46)$$

Evaluation of these integrals is straightforward.

The zero-order solution (46) is dependent on the three parameters x_*, δ and ε. The conditions that the surface Mach numbers on either side of the shock satisfy the Rankine-Hugoniot normal shock relations and that $M = 1$ at the top of the shock (point b in Fig. 10) are sufficient for their determination. As a first approximation, the surface entropy change across the shock given by Eq.(35) can be incorporated by imposing a decreasing linear variation of ΔS over the segment bc in Fig. 10. This segment corresponds to the downstream side of the shock.

The zero-order surface Mach number distribution for t=0.15 is shown in Fig. 15 for transonic conditions that include a shock wave. The analytically predicted shock location lies downstream of that predicted by the coarse-grid CFD solution, although the numerical shock is smeared over a number of surface nodes. Mach number contours are shown in Fig. 16 for t=0.10 and $M_\infty = 0.85$. The value of δ (i.e., the shock height) is 0.35. Note that the vertical scale in Fig. 16 is magnified. The basic flowfield structure has been accurately modeled by the solution of a linear homogeneous system of equations.

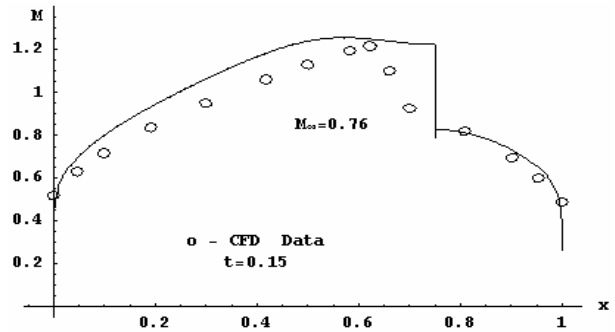

Fig. 15 Comparison of Surface Mach Number Predictions

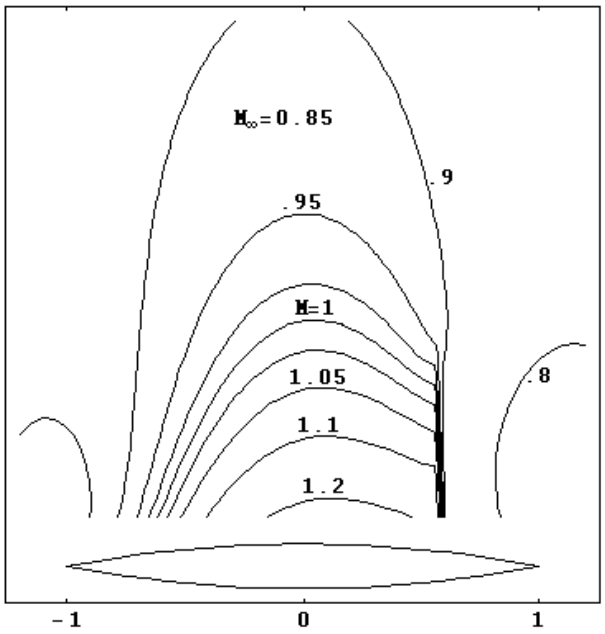

Fig. 16 Transonic Mach Number Contours

8 Summary

A new compact formulation for the 2D steady Euler equations in the physical plane is presented along with an efficient solution procedure. The Euler equations are reduced to a linear, constant-coefficient, non-homogeneous Cauchy-Riemann system. A complex-variable transformation further contracts the Euler system into a single first-order equation in the complex plane. This non-homogeneous PDE can be analytically solved at each order of approximation by iterative correction using lower-order-solution results.

The dependent variables are flow angle and logarithm of isentropic momentum magnitude relative to free stream value. The latter variable incorporates a substantial portion of the (nonlinear) flowfield compressibility effects. Surprisingly accurate compressible flow-field solutions can therefore be obtained from the (zero-order) solution of the homogeneous portion of the equations (typically a linear boundary-value problem on a simple domain). This choice of dependent variables offers distinct advantages over more conventional variable choices in terms of boundary condition imposition and solution accuracy.

Results are presented for the simple case of compressible flow past a circular cylinder to demonstrate the solution procedure and its accuracy. They agree well with sub-critical analytical results from an earlier asymptotic analysis. The solution template for the circular cylinder is extended to airfoil geometries. Analytical airfoil results compare favorably with CFD predictions. A remarkably accurate prediction of critical Mach number is obtained from the zero-order solutions.

A very local shock-like mapping is introduced that provides a mechanism for describing transonic flow with an embedded shock wave. The Rankine-Hugoniot shock relations are approximately enforced (at zero order) across the shock to demonstrate the procedure. Results are presented for a thin bi-convex airfoil at transonic conditions and comparison with CFD predictions validates the shock formation procedure.

The author would like to thank Dr. J. Shim for providing the CFD results shown herein.

9 References

1. Verhoff, A., “Global Far-Field Computational Boundary Conditions for C- and O-Grid Topologies,” AIAA Journal, Vol. 36, No. 2, Feb. 1998, pg. 148-156.
2. Verhoff, A., and Cary, A., “An Analytical Asymptotic Solution Method for 2D Transonic Inviscid Flow,” AIAA Paper No. 99-0173, Jan. 1999.
3. Verhoff, A., “Analytical Euler Solution for Two-Dimensional Compressible Ramp Flow With Experimental Comparison,” AIAA Journal, Vol. 42, No.5, May 2004, pg. 997-1008.
4. Verhoff, A., “Analytical Euler Solution for 2D Compressible Airfoil Flow,” AIAA Paper No. 03-0427, Jan. 2003.
5. Lighthill, M.J., Higher Approximations in Aerodynamic Theory, Sec. E, Princeton Univ. Press, 1960.
6. Liepmann, H.W., and Roshko, A., Elements of Gasdynamics, Wiley, 1957.